Precursor-derived rare earth metal pyrochlores: $Nd_2Sn_2O_7$ nanofibers and thin films as efficient photoabsorbers

*Aida Jamil, Johannes Schläfer, Yakup Gönüllü, Ashish Lepcha and Sanjay Mathur**

Institute of Inorganic Chemistry, University of Cologne

Greinstraße 6, D-50939 Cologne, Germany

Keywords: Rare Earth Metal, Tin, Germanium, Lead, Alkoxide, Electrospinning, PEC, photocatalyst

ABSTRACT

Single phase rare earth pyrochlores, $Ln_2M_2O_7$, were produced as nanofibers and thin films by electrospinning and spin-coating of chemical sols obtained from bimetallic metal-organic precursors, $Ln^{III}M^{II}(O^tBu)_5Py$ (Ln^{III} = La, Pr, Nd, Sm, Er, Yb; M^{II} = Ge, Sn, Pb; Py = pyridine). Compatibility of the metal ratio in the single-source compounds was confirmed by single crystal X-ray diffraction analyses and the ratio was preserved during the processing as the crystalline pyrochlore materials originated from an amorphous preceramic aggregate as confirmed by powder XRD and TEM studies. The photocatalytic activity of the $Nd_2Sn_2O_7$ nanofibers was found to be significantly higher than that of TiO_2. $Nd_2Sn_2O_7$ thin films deposited on F:SnO_2 as bilayered $Nd_2Sn_2O_7$//Fe_2O_3 photoanodes showed superior photoelectrochemical (PEC) efficiency

for water splitting reaction with an over three-fold higher photocurrent density than bare Fe_2O_3 photoanodes.

INTRODUCTION

Photocatalysts based on metal oxide semiconductors such as TiO_2,[1] Fe_2O_3[2-5] or WO_3[6] have received sizeable attention as potential photoanode materials for photoelectrochemical water splitting (PEC) and as catalysts for the photodegradation of organic pollutants. Albeit tremendous efforts, most photocatalysts still face major shortcomings such as poor solar absorption efficiency, photocorrosion, high recombination of charge carriers and unsatisfactory surface kinetics. In this context, immense efforts are dedicated towards optimization of electrodes by improving the structural and electronic properties of the corresponding metal oxides through mixing of electronic states of individual metals. Nanostructured oxide semiconductors are promising photocatalysts due to their distinctive properties offering several advantages over their bulk counterparts such as short diffusion lengths of charge carriers, high reflectivity and rich defect and structural chemistries.

In this context, bimetallic oxides are of substantial interest due to their unique functional properties (piezoelectricity[7] luminescence[8]) and cooperative effects (e.g., multiferroicity[9]) emerging from the presence of different metallic centers in the crystal structure. Rare earth metal stannates of the general formula $Ln_2Sn_2O_7$ (Ln = La-Yb) build up by an interwoven 3d network of corner-linked SnO_6 octahedra and LnO_8 edge-sharing cubes. They are attractive candidates for catalytic applications due to their high temperature stability and defect structure.[10, 11] Compared to several other bimetallic oxides such as spinels (AB_2O_4), perovskites (ABO_3) and garnets ($A_3B_5O_{12}$), pyrochlores ($A_2B_2O_7$) are less investigated for photocatalytic applications. Usually,

lanthanide stannates are prepared by traditional solid-state methods, which require high temperatures accompanied by several grinding and heating steps in order to minimize phase-heterogeneities.[10-12]

Recently, few synthesis strategies have been developed for the fabrication of $Ln_2Sn_2O_7$ nanoparticles by chemical phase approaches, such as sol–gel, aerosol pyrolysis, co-precipitation, chemical solution deposition and combustion approaches.[13-15] For example, *Wang et al.* reported a soft-chemical hydrothermal synthesis starting from an inorganic metal to produce pyrochlores as well-dispersed highly crystalline nanocubes. However, the reaction is very sensitive to the concentration of mineralizer (e.g., NaOH) and requires high pressures.[16-19] **Fehler! Verweisquelle konnte nicht gefunden werden.Fehler! Verweisquelle konnte nicht gefunden werden.** In view of the above, development of new preparation methods, especially those enabling a phase-selective synthesis and lower temperatures are highly desirable.

Heterobimetallic metal alkoxides are widely established precursors for the synthesis of ternary oxides due to pre-existent metal-oxygen bonds, pre-defined cationic ratios and consistent physicochemical properties. In addition, they are easily accessible by mixing two different metal alkoxides in which the more acidic metal alkoxide attracts one or more alkoxo ligands under formation of an anionic alkoxometallate unit, $\{M_y(OR)_x\}^{z-}$. This unit can act as a polydentate, chelating ligand which coordinates the more electropositive metal center forming stable heterobimetallic complexes.[20]

The stability of such polymetallic arrangements which is decisive for the formation of the solid-state-phase usually increases with increasing difference in electronegativity of both metals, a phenomenon that was first described for metal hydroxides by *Meerwein*.[21] The alkoxostannate unit $\{Sn(O^tBu)_3\}^-$ exhibiting a ψ^1-pseudo-tetrahedral coordination environment, is a versatile

ligand that allows accommodating varying metal cations across the whole periodic table. Depending on the ionic radius and electronegativity of the heterometal, the $\{Sn(O^tBu)_3\}^-$ unit can bind either in a bidentate (κ^2) or tridentate (κ^3) fashion.[22-28] Surprisingly, the reaction of $\{Sn(O^tBu)_3\}^-$ with trivalent lanthanides has not been reported so far which stimulated our interest in extending the chemistry of mixed-metal compounds containing main group and lanthanide elements and to evaluate their potential in materials synthesis.

In this study, we report the synthesis and characterization of heterobimetallic alkoxide precursors based on lanthanide and main group elements. In particular, alkoxostannate complexes based on the chelation of anionic $\{Sn(O^tBu)_3\}^-$ unit to different rare earth metals were systematically investigated to study the influence of heterometal partner and ratio on the molecular structure. Moreover, the Nd-Sn compound, $[NdSn(O^tBu)_5(Py)]$, was used to electrospun nanofibers and or spin-coat thin films of $Nd_2Sn_2O_7$ for solar harvesting applications. While single $Nd_2Sn_2O_7$ layer did not present any photoactivity in PEC measurements, its heterostructures with Fe_2O_3 yielded an over 3 fold enhancement in photocurrent when compared to the single Fe_2O_3 layer.

RESULTS AND DISCUSSION

Synthesis of Heterometallic *tert*-Butoxides

Heterobimetallic *tert*-butoxides $[LnSn(O^tBu)_5(Py)]$ (Ln = La, Pr, Nd, Sm, Er, Yb; **1a-f**) were synthesized by mixing homometallic $[Sn_2(O^tBu)_4]$ with two equivalents of $[Ln\{N(SiMe_3)_2\}_3]$ in a toluene-pyridine mixture followed by the addition of *tert*-butanol. Pyridine was added in order to saturate the coordination sphere around the lanthanide center that would otherwise be fivefold coordinated. Upon mixing a color change to orange which is characteristic for the homoleptic tin(II) amide $[Sn\{N(SiMe_3)_2\}_2]$ was observed that indicated a ligand redistribution. The amido

ligands were replaced by adding an excess of *tert*-butyl alcohol and heating the reaction mixture at 70 °C (30 min) to obtain **1a-f** in good yields (47-76%).

The molecular structure of the stannate complexes in solution was exemplary studied for the diamagnetic lanthanum derivative by NMR spectroscopy. The ^{1}H NMR spectrum of **1a** showed two overlapping resonances at 1.43 and 1.46 ppm, which could be assigned to the terminal and μ_2-bridging alkoxo groups, respectively. In the aromatic region three separate multipletts were detected that correspand to the pyridine ligand which is coordinated to the La center. The resonance of the μ_2-bridging *tert*-butoxo groups (1.46 ppm) assigned by an ^{1}H, ^{119}Sn HMBC experiment showed a correlation to the Sn(II) center. The ^{119}Sn chemical shift at -211 ppm is characteristic for a ψ^1-pseudo-tetrahedral $\{Sn(OR)_3\}^-$ alkoxometallate ligand chelating a heterometal in a tridentate fashion. The spectroscopic data suggested a rigid bimetallic structure in solution with the La center octahedrally coordinated by a $\{Sn(O^tBu)_3\}^-$-unit, two *tert*-butoxo groups and one pyridine ligand. This was supported by integration of the proton resonances showing a pyridine: alkoxo ligand ratio of 1:5.

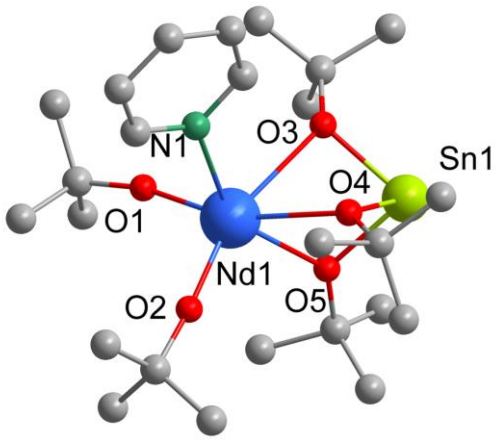

Figure 1: Molecular Structure of [NdSn(O^{t}Bu)$_5$(Py)] (**1c**). The hydrogen atoms have been omitted for clarity**. Selected bond lengths in [Å]: Nd-O$_{terminal}$ 2.136, Nd-O$_{\mu2}$ 2.500, Nd-N 2.609, Sn-O 2.086, Nd-Sn 3.336.**

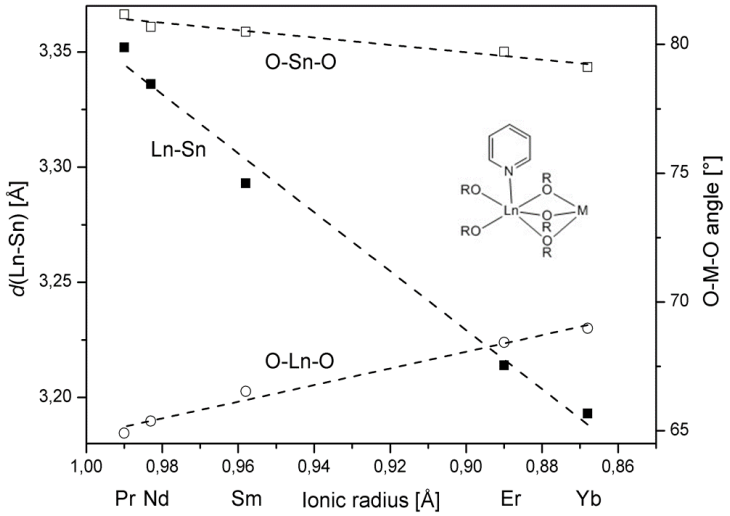

Scheme 1: Correlation of rare earth metal ionic radii[29] with selected bonding parameters. Ln: La, Pr, Sm, Er, Yb; M = Sn, Pb Average bond lengths and metal-metal distances in [Å] for complexes **1b** Pr-$O_{terminal}$ 2.140, Pr-$O_{\mu 2}$ 2.524, Pr-N 2.638, Sn-O 2.082, Pr-Sn 3.352, **1d** Sm-$O_{terminal}$ 2.123, Sm-$O_{\mu 2}$ 2.463, Sm-N 2.551, Sn-O 2.091, Nd-Sn 3.293, **1e** Er-$O_{terminal}$ 2.056, Er-$O_{\mu 2}$ 2.383, Er-N 2.469, Sn-O 2.090, Er-Sn 3.214, **1f** Yb-$O_{terminal}$ 2.043, Yb-$O_{\mu 2}$ 2.353, Yb-N 2.438, Sn-O 2.092, Yb-Sn 3.193 and **2b** Nd-$O_{terminal}$ 2.152, Nd-$O_{\mu 2}$ 2.470, Nd-N 2.611, Pb-O 2.203, Nd-Pb 3.380.

Single crystal X-ray diffraction analysis of complexes **1b-f** revealed that **1b**, **1c** and **1e** were isostructural and crystallized in the triclinic space group $P\,1^{-}$(Z =2), whereby complexes **1d** and **1f** crystallized in the orthorhombic crystal system with two crystallographic independent molecules in the asymmetric unit (*P cab*, Z = 16). The molecular structures of all complexes consisted of a bimetallic metal-organic framework based on a tri-dentate coordination of the $\{Sn(O^tBu)_3\}^-$ ligand to the lanthanide center (Figure 1). The strong polydentate linkage resulted in short metal-metal distances (d_{MM}) which show a linear trend when plotted against the corresponding ionic radii (Scheme 1). The bite angle of the stannate ligand was found to increase with increasing atomic numbers showing the flexibility of the alkoxometallate group to accommodate metal ions of different sizes. In contrast, the Sn-O distances remained unchanged in all complexes, which consequently resulted in decreased mean O-Sn-O angles. The Ln-O bond lengths of the bridging ligands match those typically found for μ_3-O^{t}Bu groups with the

trans-standing *tert*-butoxo group showing a shorter Ln-O distance due to the structural *trans*-effect caused by the pyridine ligand.[30]

$[Ge_2(O^tBu)_4]$ and $[Pb_3(O^tBu)_6]$ reacted in an analogous manner to the tin(II) compound as verified by the successful synthesis and structural analysis of germanium and lead derivatives. The lead complex $[NdPb(O^tBu)_5(Py)]$ (**2d**) resembled the tin derivatives, whereas for the germanium compound two superimposing molecular structures were found in the asymmetric unit, $[NdGe(O^tBu)_5(Py)]$ (**2a**) and $[NdGe(O^tBu)_5(HO^tBu)(Py)]$ (**2a'**) (Figure 2). The individual germanium atoms Ge1A **(2a**) and Ge1B (**2a'**) reside on two different atomic positions with a site occupation factor of 0.5, respectively. The atom sites of the terminal *tert*-butoxo group (O6-C64) are only half-occupied, all other ligand sites and the Nd site exhibited a full occupancy. The coexistence of both complexes (1:1 ratio) in the solid state was supported by elemental analysis which is in good agreement with a 1:1 mixture (Anal. Calcd **2a**: C 45.39, H 7.62, N 2.12; **2a**': C 47.35, H 8.22, N 1.90; **2a/2a'**: C 46.37, H 7.92, N 2.01; Found: C 46.15, H 7.43, N 1.99).

2a adopted the already described tridentate coordination motif whereas in complex **2a'** the metal atoms are only connected by two alkoxo groups. The coordination sphere on the neodymium atom is completed by an additional *tert*-butanol ligand forming an intramolecular hydrogen bridge to the terminal *tert*-butoxo ligand on the germanium atom. Due to the superposition of both structures it was not possible to discriminate whether the alcohol ligand is located on the neodymium or germanium center and also a discussion of metal-oxygen bonds is not reasonable. The formation of hydrogen bonds in metal alkoxides is a well-known phenomenon which was already described for the rare earth aluminates and ferrates $[Ln_2M_2(O^iPr)_{12}(HO^iPr)_2]$ (M = Al, Fe)[31] but it has been unknown until now for the more crowded *tert*-butoxide complexes. The metal-metal distance observed for the bimetallic complexes

[NdM(O^{t}Bu)$_5$(Py)] was found to decrease with decreasing ionic radius of the main group metal (**1c**: 3.336 Å, **2a**: 3.380 Å and **2b**: 3.064 Å).

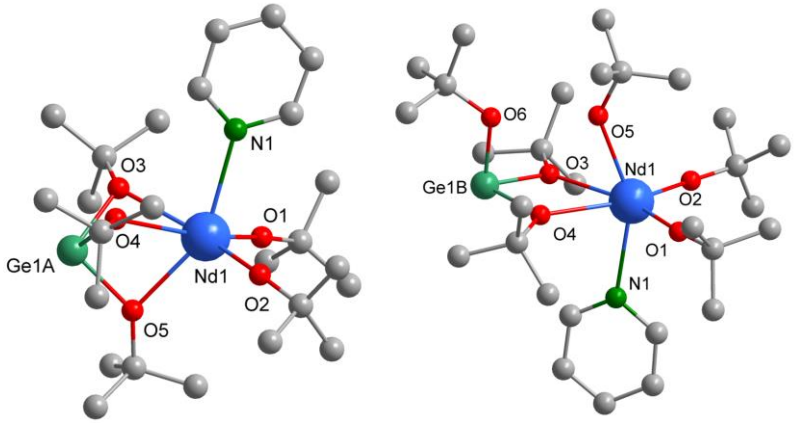

Figure 2: Molecular Structure of [NdGe(O^{t}Bu)$_5$(Py)] (**2a**) and [NdGe(O^{t}Bu)$_5$(Py)(HO^{t}Bu)] (**2a'**). The hydrogen atoms have been omitted for clarity. Selected bond lengths in [Å]: Nd-$O_{terminal}$ 2.135, Nd-$O_{\mu 2}$ 2.477, Nd-N 2.602, Ge-O 1.968 (1.909), Nd-Ge 3.064 (3.682).

[NdSn$_2$(O^{t}Bu)$_7$] **3** was isolated as sublimable (10^{-2} mbar at 140 °C) pale blue crystals by reacting neodymium amide with tin(II) alkoxide in the absence of pyridine. The molecular structure revealed the coordination of two {Sn(O^{t}Bu)$_3$}$^-$ ligands to the central Nd atom in a tridentate (Sn1, κ^3) and bidentate (Sn2, κ^2) fashion, respectively (Figure 3). The complex crystallized in the rhombohedral lattice system with the Nd:Sn vector of the κ^3-alkoxostannate unit located on a three-fold rotation axis. A comprehensive structure solution was difficult due to disordered cationic sites, however, the data could be refined to obtain metal-ligand connectivity (Figure 3).

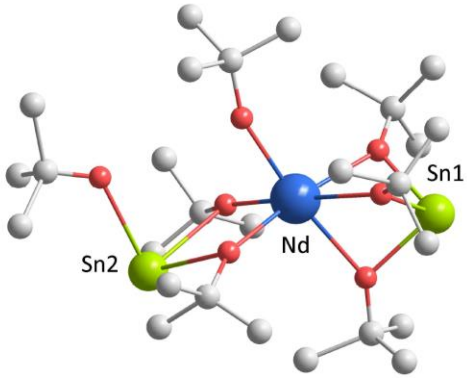

Figure 3: Molecular structure motif of [$NdSn_2(O^tBu)_7$] (**3**). Hydrogen atoms have been omitted for clarity.

Table 1: Crystal and structure refinement data for **1a-e**.

compound	**1b**	**1c**	**1d**	**1e**
formula	$PrSnC_{25}H_{50}NO_5$	$NdSnC_{25}H_{50}NO_5$	$SmSnC_{25}H_{50}NO_5$	$ErSnC_{25}H_{50}NO_5$
M_r /gmol^{-1}	704.26	707.59	713.70	730.61
cryst. syst.	triclinic	triclinic	orthorhombic	triclinic
space group	$P\bar{1}$	$P\bar{1}$	*P cab*	$P\bar{1}$
T /K	293(2)	170(2)	170(2)	293(2)
a /Å	9.8942(6)	9.744(5)	18.074(5)	9.806(5)
b /Å	10.1449(6)	9.944(5)	21.596(5)	10.856(5)
c /Å	17.2413(10)	17.140(5)	33.002(5)	16.213(5)
α /°	87.136(5)	87.209(5)	90.00	88.152(5)
β /°	84.379(5)	84.319(5)	90.00	86.039(5)
γ /°	77.735(5)	77.761(5)	90.00	73.883(5)
V /Å^3	1682.22(17)	1614.4(13)	12882(5)	1654.0(12)
Z	2	2	16	2
μ (Mo-K_α) /mm^{-1}	2.201	2.392	1.822	3.302
No. of unique rflns, R_{int}	7123, 0.0701	6869, 0.1184	10817, 0.1232	7025, 0.0692
goodness of fit	1.051	1.107	2.610	1.054
final R indices [$I>2\sigma(I)$]: R_1, wR_2	0.0286, 0.0754	0.0271, 0.0601	0.0437, 0.1314	0.0335, 0.0870
R indices (all data): R_1, wR_2	0.0318, 0.0771	0.0296, 0.0648	0.0572, 0.1437	0.0367, 0.0891
Residual e density	0.937, -1.047	0.709, -0.856	5.019, -1.951	2.062, -1.695

Table 2: Crystal and structure refinement data for **1f**, **2a-b** and **4**.

compound	**1f**	**2a/2a'**	**2b**	**4**
formula	$YbSnC_{25}H_{50}NO_5$	$Nd_2Ge_2C_{54}H_{109}N_2O_{11}$	$NdPbC_{25}H_{50}NO_5$	$Nd_2Sn_2C_{36}H_{86}O_{12}$
M_r /gmol^{-1}	736.39	1396.13	796.09	1236.90
cryst syst	orthorhombic	monoclinic	monoclinic	triclinic
space group	*P cab*	*C* 2/*c*	*P* 2$_1$/*n*	$P\bar{1}$
T /K	170(2)	170(2)	170(2)	170(2)

a /Å	17.9118(5)	12.6722(4)	9.651(5)	9.8856(4)
b /Å	21.4320(7)	15.2056(3)	16.524(5)	10.0611(4)
c /Å	32.6856(8)	35.5907(11)	21.132(5)	14.7887(6)
α /°	90.00	90.00	90.00	71.950(3)
β /°	90.00	95.924(2)	102.478(5)	71.345(3)
γ /°	90.00	90.00	90.00	78.260(3)
V /Å^3	12547.5(6)	6821.3(3)	3290(2)	1316.10(10)
Z	16	4	4	1
μ (Mo-K_α) /mm^{-1}	3.789	2.421	6.698	2.924
No. of unique rflns, R_{int}	13333, 0.1580	5730, 0.0895	6980, 0.1198	7096, 0.1047
goodness of fit	0.899	1.316	1.019	1.043
final R indices [$I>2\sigma(I)$]: R_1,	0.0562, 0.1332	0.0589, 0.1441	0.0389, 0.0947	0.0541, 0.1403
R indices (all data): R_1, wR_2	0.1146, 0.1626	0.0631, 0.1467	0.0594, 0.1040	0.0591, 0.1456
Residual e density	2.750, -1.591	1.059, -0.935	2.387, -1.456	4.041, -2.759

Electrospinning of $Nd_2Sn_2O_7$ nanofibers

A spin solution was prepared by mixing [$NdSn(O^tBu)_5(Py)$] and polyvinylpyrrolidone (PVP) as spinning-aid, in isopropyl alcohol. The replacement of bulkier *tert*-butoxo ligands by more compact iso-propoxo groups resulted in a condensation of the dimeric alkoxide to the tetranuclear heterometallic alkoxide [$Nd_2Sn_2(O^iPr)_{10}(HO^iPr)_2$] **4** still exhibiting the adequate Nd:Sn ratio. In the centrosymmetric molecular structure, the coordination sphere of each of the neodymium atoms is completed by one $\{Sn(O^iPr)_3\}^-$ ligand coordinating in a bidentate fashion and one *iso*-propanol group. Further, an additional stabilization is achieved by the formation of intramolecular hydrogen bridges of the acidic proton of the *iso*-propanol ligand coordinating the neodymium atoms and the terminal alkoxo group of the stannate unit. The reaction of Nd-Sn alkoxo species with subsequently added carboxylic acid produced *in-situ* oxo-clusters and the intermolecular condensation reaction became evident in the increasing viscosity of the spinning sol.

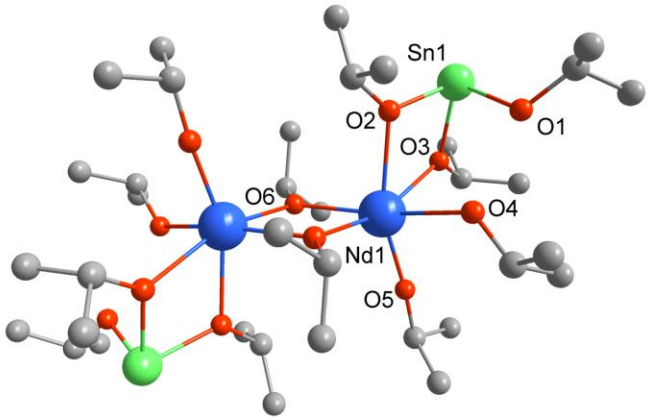

Figure 4: Molecular structure of $[Nd_2Sn_2(O^iPr)_{10}(HO^iPr)_2]$ (**4**). The hydrogen atoms have been omitted for clarity. Selected bond lengths [Å]: Sn-O(1) 2.062(4), Sn-O(2) 2.075(5), Sn-O(3) 2.094(3), Nd-O(4) 2.493(4), Nd-O(5) 2.131(4), Nd-O(6) 2.348(4), Sn-Nd 3.659(1), Nd-Nd 3.790(1).

The XRD pattern of the nanofibers calcined in air for 3h at 800 °C showed broad reflexes whichcould be assigned of the $Nd_2Sn_2O_7$ pyrochlore phase. The formation of $Nd_2Sn_2O_7$ was accompanied by simultaneous oxidation of the bivalent tin. The transmission electron micrograph of the calcined fibers displayed nanofibers with diameters between 20-40 nm and a porous structure constituted by crystalline $Nd_2Sn_2O_7$ nanoparticles with a mean size of 10 nm (Figure 5).

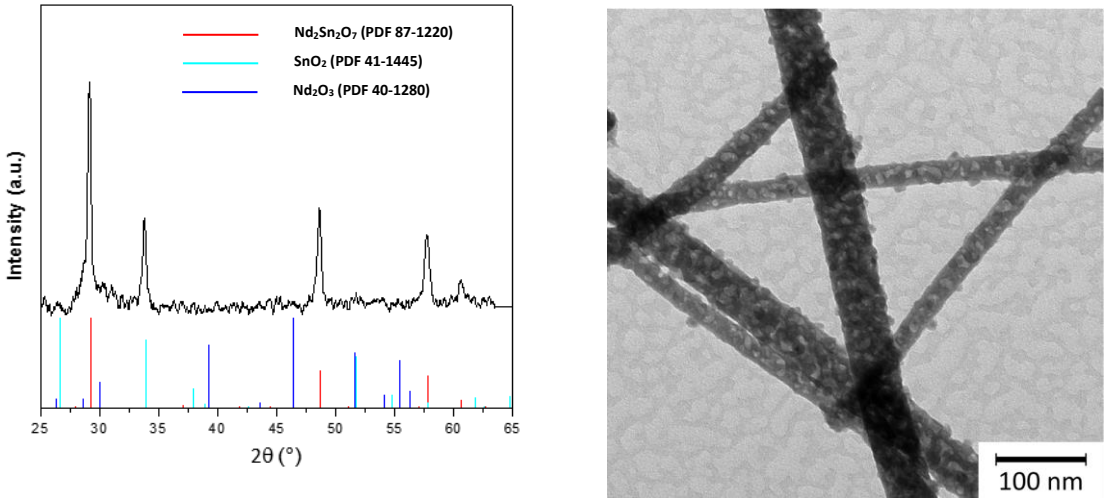

Figure 5: XRD pattern (left) and TEM image (right) of polycrystalline $Nd_2Sn_2O_7$ nanofibers.

Pyrochlore $A_2B_2O_7$ and δ-phase $A_4B_3O_{12}$ compounds are related to the fluorite structure,[32] which form over a large compositional space due to the flexibility of the structure (Figure 6).[33] Apparently, the use of single-source bimetallic precursors solely formed pyrochlore type $Nd_2Sn_2O_7$ possibly due to a templating effect caused by the chemical homogenization of the preceramic homogenate through the pre-existent Nd-OR-Sn-unit and the pre-defined Nd:Sn (1:1) ratio.

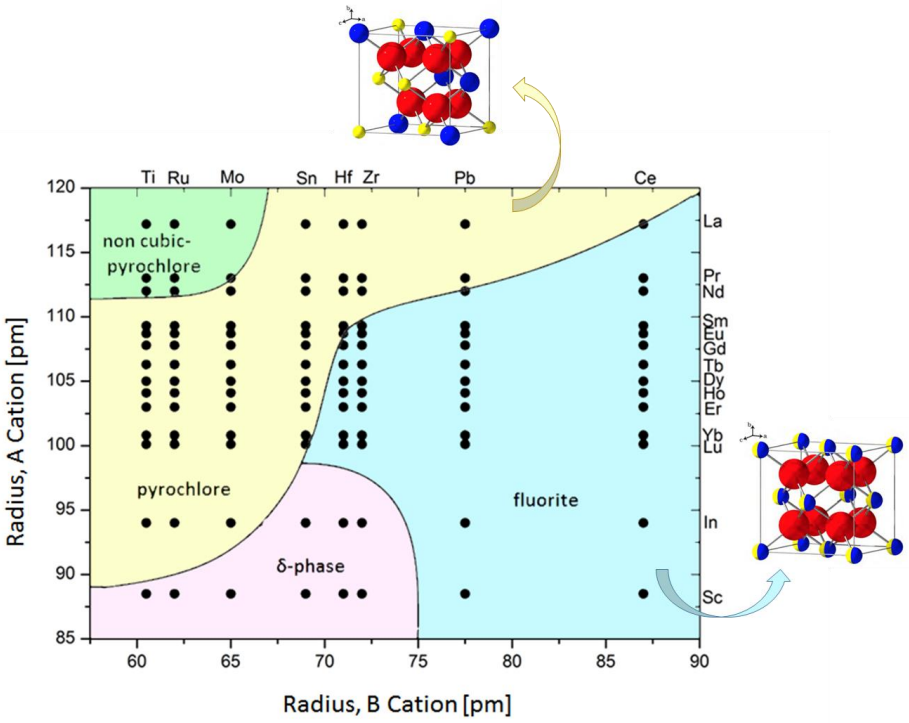

Figure 6: Phase map showing the stability of cubic pyrochlore $A_2B_2O_7$ (yellow), non-cubic pyrochlore $A_2B_2O_7$ (green), disordered fluorite $(AB)_2O_7$ (blue) and δ-phase $A_4B_3O_{12}$ (red) at high temperatures as a function of cation radii. A is a trivalent cation and B is a tetravalent cation. Larger blue spheres are A^{3+} ions, small yellow spheres are B^{4+} ions and large red spheres are O^{2-} ions in the unit cell.[32]

Photocatalytic Properties of $Nd_2Sn_2O_7$ nanofibers

Photooxidation properties of $Nd_2Sn_2O_7$ nanofibers were demonstrated against a TiO_2 reference in a methylene blue (MB) solution ($c_{MB} = 3.62 \cdot 10^{-5}$ mol/L). For spectrophotometric studies and dye degradation kinetics 2.959 mg ($c_{cat.} = 4.64 \cdot 10^{-5}$ mol/L) $Nd_2Sn_2O_7$ nanofibers were dispersed

into a quartz tube filled with 100 mL of the MB solution followed by irradiation with UV-light (15 W, 352 nm; Figure 7, left).

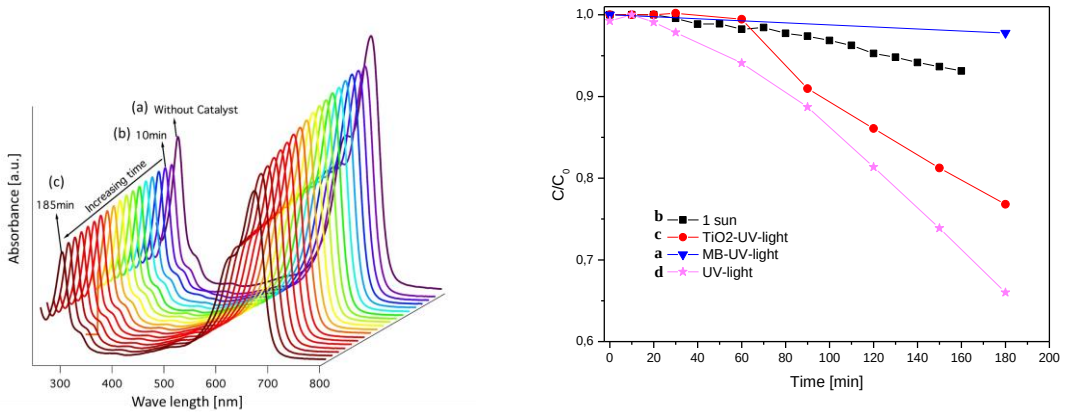

Figure 7: UV-vis spectra (left), degradation curves of MB solutions irradiated under ultraviolet light: (a) without $Nd_2Sn_2O_7$ for 180 min, (b-c) with $Nd_2Sn_2O_7$, for 10 min (b) and for 180 min (c). The degradation rate (C/C_0) of MB as a function of irradiation time (right), (a) without $Nd_2Sn_2O_7$ under UV-light; (b) with $Nd_2Sn_2O_7$ under sunlight; (c) with TiO_2 under UV-light and (d) with $Nd_2Sn_2O_7$ under UV-light.

Comparison of the photooxidation behavior of $Nd_2Sn_2O_7$ with the typically used TiO_2-MB solution confirmed the higher photoactivity and superior performance of $Nd_2Sn_2O_7$ nanofibers (Figure 7, right). In addition to irradiation with ultraviolet light, photodegradation studies were also conducted under 1 sun illumination (150 W Xenon lamp (Oriel), equipped with a 1.5 AM filter) (line **b**) however, the overall photocatalytic activity was found to be low due to the large band gap of $Nd_2Sn_2O_7$ (3.5-4.5 eV)[34]. Wang et al. reported the $La_2Sn_2O_7$ nanoparticles present similar behavior as reported in this work.[17] The photostability of $Nd_2Sn_2O_7$ was exploited to in conjunction with hematite thin films towards photoelectrochemical splitting of water. For this purpose, hematite films were grown onto FTO substrates by plasma-enhanced chemical vapor deposition (PE-CVD), as reported elsewhere[35] using iron pentacarbonyl $Fe(CO)_5$ and oxygen gas. $Nd_2Sn_2O_7$ films were deposited onto the Fe_2O_3 layer via a spin-coating process by using the precursor **1c** from a solvent mixture (toluene, pentane and isopropanol) and annealed in air at

750 °C to produce hetero-junctioned $Nd_2Sn_2O_7$//Fe_2O_3 bilayers. The cross section SEM investigation of the $Nd_2Sn_2O_7$ structures exhibited that the porous structure evident in in-plane SEM micrographs (Figures 8b and c) is also mentioned within the films that showed typically the thickness to be approximately 4μm (Figure 8a).

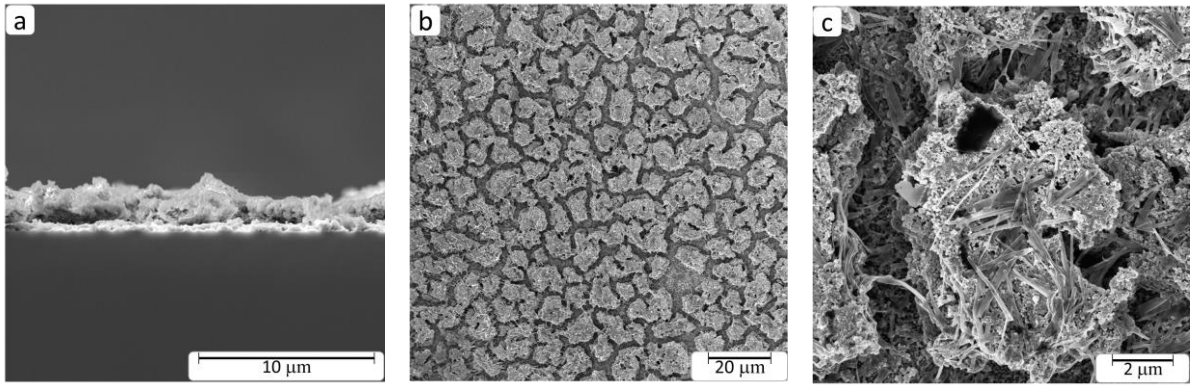

Figure 8: (a) Cross section SEM image and top view SEM images with (b) lower and (c) higher magnification of **$Nd_2Sn_2O_7$** photoanodes**.**

Photoelectrochemical measurements were carried out in a three electrode electrochemical cell working with a 1.0 M NaOH electrolyte under 1 sun illumination (150 W Xenon lamp (Oriel), equipped with a 1.5 AM filter) and using a potentiostat (PAR, Model: Versa state IV, USA). Potentials were calculated with respect to the reversible hydrogen electrode (RHE) scale using the *Nernst* equation (1).

$$E_{RHE} = E_{SCE} + E^0_{SCE} + 0.059pH \quad \text{.....1}$$

The comparison of photoelectrochemical activities of the single (**$Nd_2Sn_2O_7$** and **Fe_2O_3**) with the bilayered (**$Nd_2Sn_2O_7$//Fe_2O_3**) electrodes evidently showed the role of the oxide-oxide interface in enhancing the overall photocurrent density (Figure 9). While the Fe_2O_3 photoanode showed known PEC behavior upon irradiation, $Nd_2Sn_2O_7$ photoanodes exhibited a photoelectron activity

only above 1.6 V where the concomitant electrolysis of water cannot be ruled out.[35] Interestingly, the $Nd_2Sn_2O_7$ overlayer on the Fe_2O_3 photoanode showed a significant advancement in PEC values (**Fe_2O_3**: 0.08 mA/cm^2 and **$Nd_2Sn_2O_7$//Fe_2O_3**: 0.21 mA/cm^2 at 1.23 V vs RHE under 1 sun illumination). This can be explained by (i) the photocatalytic effect of the $Nd_2Sn_2O_7$ layer and the large band gap that inhibits the backward migration of holes in the films ii) or by the high UV absorption of $Nd_2Sn_2O_7$//Fe_2O_3 planar heterostructure (Figure 9) due to the high band gap energy of $Nd_2Sn_2O_7$ (3.5 eV)[36] which results in high energetic electrons and holes.

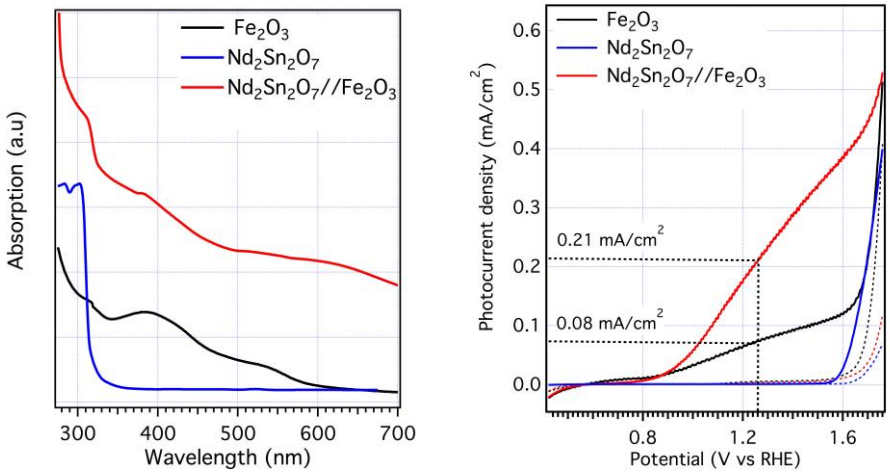

Figure 9: (left) UV-vis spectra and (right) photoelectrochemical measurements of single and multilayer photoanodes. (dot lines present the PEC measurements in dark)

CONCLUSION

The synthesis of heterobimetallic alkoxide precursors [LnM(O^{t}Bu)$_5$(Py)] (Ln = La, Pr, Nd, Sm, Er, Yb; M = Ge, Sn, Pb) comprising a predefined metal-metal ratio suitable for the formation of bimetallic rare earth metal pyrochlores is reported. The flexibility of combining lanthanide cations as well as group 14 metals over a broad range under retention of the molecular structure was demonstrated as molecular structural concept. For the first time, the synthesis of porous $Nd_2Sn_2O_7$ nanofibers starting from single-source precursors was demonstrated. The $Nd_2Sn_2O_7$

nanofibers exhibited a high photocatalytic activity superior than that of the well-known photocatalyst TiO_2. Moreover, the photoelectrochemical investigations showed that $Nd_2Sn_2O_7$ films in combination with Fe_2O_3 layers are promising photoanode materials capable of producing a 3 fold higher photocurrent density when compared to bare Fe_2O_3 films.

EXPERIMENTAL SECTION

Precursor Synthesis

General Remarks. If not mentioned differently all reagents and solvents were used without further purification. All reactions and manipulations were carried out under dry nitrogen gas using a *Stock*-type all glass vacuum line or under argon atmosphere in a glovebox (MBraun); solvents, alcohols and pyridine were dried over sodium or CaH_2 and were distilled prior to use. $[Ln\{N(SiMe_3)_2\}_3]$[36] and $[M_x(O^tBu)_{2x}]$ (x = 2, M = Sn[37], Ge[28]; x = 3, M = Pb[28] were synthesized according to literature methods. NMR spectra were recorded on a Bruker Avance II 300 spectrometer. ^1H (300.1 MHz), ^{13}C (75.7 MHz) and ^{119}Sn (111.9 MHz) chemical shifts are reported in parts per million relative to external tetramethylsilane or $SnMe_4$ and are referenced internally to the proton impurity or ^{13}C signal of the solvent, respectively. Elemental analyses were carried out on a HEKAtech CHNS Euro EA 3000. The sample preparation was performed in a glove box whereas the reweighing of the cartridges was done outside under environmental atmosphere. Deviations of the CHNS data from the calculated values could be attributed to the extraordinary sensitivity of the compounds.

Data collection for X-ray structure elucidation was performed on a STOE IPDS 2T diffractometer using graphite-monochromated MoKα radiation (0.71071 Å). The programs used in this work are STOE's X-Area[38] and the WINGX suite of programs[39], including SIR-92[40],

SHELX & SHELXTL[41] and PLATON[42] for structure solution and refinement. H-atoms were calculated geometrically and a riding model was applied during the refinement process.

General reaction procedure for synthesis of 1a-f and 2a-b. In a typical reaction a solution of 1 eq [Ln{N(SiMe$_3$)$_2$}$_3$] in toluene was mixed with a solution of 1/*n* eq of the corresponding alkoxide [M$_n$(O^{t}Bu)$_{2n}$] in toluene (20-30 mL) followed by the addition of an excess of pyridine (1-2 mL). After stirring for 30 min at room temperature an excess of *tert*-butanol (2-3 mL) was added and the reaction mixture was heated to 70 °C for 2 h. All volatiles were removed under reduced pressure and the crude product was purified by recrystallization from a toluene solution.

Synthesis of 1a. 0.50 g (0.8 mmol) of [La{N(SiMe$_3$)$_2$}$_3$] and 0.21 g (0.5 mmol) [Sn$_2$(O^{t}Bu)$_4$] were reacted to give 0.33 g (58%) of [LaSn(O^{t}Bu)$_5$(Py)] in form of colourless crystals by recrystallization from toluene. ^{1}H NMR (C$_6$D$_6$, 25 °C): δ 1.43 (s, 27H, terminal O^{t}Bu), 1.46 (s, 18H, μ_2-O^{t}Bu), 6.65 (m, 2H, *meta*-H), 6.91 (m, 1H, *para*-H), 8.77 (m, 2H, *ortho*-H). ^{13}C NMR (C$_6$D$_6$, 25 °C): δ 34.4 (terminal OC(**C**H$_3$)$_3$), 34.8 (μ_2-OC(**C**H$_3$)$_3$), 71.6 (terminal O**C**(CH$_3$)$_3$), 72.4 (μ_2-O**C**(CH$_3$)$_3$), 123.1 (*meta*-C), 135.6 (*para*-C), 149.6 (*ortho*-C). ^{119}Sn NMR (C$_6$D$_6$, 25 °C): δ -211. Anal. Calcd LaSnC$_{25}$H$_{50}$NO$_5$: C 42.76, H 7.18, N 1.99. Found: C 42.94, H 6.62, N 1.39.

Synthesis of 1b. 0.99 g (1.6 mmol) of [Pr{N(SiMe$_3$)$_2$}$_3$] and 0.42 g (0.8 mmol) [Sn$_2$(O^{t}Bu)$_4$] were reacted to give 0.53 g (47%) of [PrSn(O^{t}Bu)$_5$(Py)] in form of bright green crystals by recrystallization from toluene. Anal. Calcd PrSnC$_{25}$H$_{50}$NO$_5$: C 42.63, H 7.16, N 1.99. Found: C 42.55, H 6.07, N 2.07.

Synthesis of 1c. 0.665 g (1.063 mmol) of [Nd{N(SiMe$_3$)$_2$}$_3$] and 0.281 g (0.531 mmol) [Sn$_2$(O^{t}Bu)$_4$] were reacted to give 0.527 g (70%) of [NdSn(O^{t}Bu)$_5$(Py)] in form of blue crystals

by recrystallization from toluene. Anal. Calcd $NdSnC_{25}H_{50}NO_5$: C 42.43, H 7.12, N 1.98. Found: C 41.49, H 6.02, N 2.39.

Synthesis of 1d. 0.70 g (1.1 mmol) of $[Sm\{N(SiMe_3)_2\}_3]$ and 0.30 g (0.6 mmol) $[Sn_2(O^tBu)_4]$ were reacted to give 0.59 g (75%) of $[SmSn(O^tBu)_5(Py)]$ in form of colourless crystals by recrystallization from toluene. Anal. Calcd $SmSnC_{25}H_{50}NO_5$: C 42.076, H 7.06, N 1.96. Found: C 43.05, H 7.58, N 1.57.

Synthesis of 1e. 1.36 g (2.1 mmol) of $[Er\{N(SiMe_3)_2\}_3]$ and 0.56 g (1.1 mmol) $[Sn_2(O^tBu)_4]$ were reacted to give 1.00 g (65%) of $[ErSn(O^tBu)_5(Py)]$ in form of pink crystals by recrystallization from toluene. Anal. Calcd $ErSnC_{25}H_{50}NO_5$: C 41.10, H 6.90, N 1.92. Found: C 41.02, H 6.09, N 1.97.

Synthesis of 1f. 0.91 g (1.4 mmol) of $[Yb\{N(SiMe_3)_2\}_3]$ and 0.37 g (0.7 mmol) $[Sn_2(O^tBu)_4]$ were reacted to give 0.78 g (76%) of $[YbSn(O^tBu)_5(Py)]$ in form of colourless crystals by recrystallization from toluene. Anal. Calcd $YbSnC_{25}H_{50}NO_5$: C 40.77, H 6.84, N 1.90. Found: C 39.94, H 7.62, N 2.09.

Synthesis of 2a. 0.477 g (0.76 mmol) of $[Nd\{N(SiMe_3)_2\}_3]$ and 0.300 g (0.76 mmol) $[Ge\{N(SiMe_3)_2\}_2]$ were reacted to give 0.387 g (73%) of $[NdGe(O^tBu)_5(HO^tBu)_{0.5}(Py)]$ in form of blue crystals by recrystallization from toluene. Anal. Calcd $NdGeC_{25}H_{50}NO_5$ **2a** C 45.39, H 7.62, N 2.12; $NdGeC_{29}H_{60}NO_6$ **2a**': C 47.35, H 8.22, N 1.90; $NdGeC_{27}H_{54.5}NO_{5.5}$ **2a/2a'**: C 46.37, H 7.92, N 2.01; Found: C 46.15, H 7.43, N 1.99.

Synthesis of 2b. 0.347 g (0.55 mmol) of $[Nd\{N(SiMe_3)_2\}_3]$ and 0.382 g (0.55 mmol) $[Pb\{N(SiMe_3)_2\}_2]$ were reacted to give 0.22 g (49%) of $[NdPb(O^tBu)_5(Py)]$ in form of blue crystals by recrystallization from toluene. Anal. Calcd $NdPbC_{25}H_{50}NO_5$: C 37.72, H 6.33, N 1.76. Found: C 37.16, H 6.18, N 1.62.

Synthesis of 3. 0.30 g (0.48 mmol) of $[Nd\{N(SiMe_3)_2\}_3]$ and 0.254 g (0.48 mmol) $[Sn_2(O^tBu)_4]$ were reacted to give 0.26 g (60%) of $[NdSn_2(O^tBu)_7]$ in form of blue crystals by recrystallization from toluene. Anal. Calcd $NdSn_2C_{28}H_{63}O_7$: C 37.64, H 7.11. Found: C 38.34, H 7.08.

Synthesis of 4. 0.507 g (0.8 mmol) of $[NdSn(O^tBu)_5(Py)]$ was dissolved in a mixture of 15 mL isopropanol and 15 mL toluene and stirred for 30 min at room temperature. All volatiles were removed under reduced pressure and the crude product was recrystallized from isopropanol/toluene mixture. 0.47 g (95%) of $[Nd_2Sn_2(O^iPr)_{10}(HO^iPr)_2]$ were obtained in form a of pale blue crystals. Anal. Calcd $Nd_2Sn_2C_{36}H_{86}O_{12}$: C 34.96, H 7.01. Found: C 34.42, H 6.67.

Deposition of the Fe_2O_3 layer. Thin film photoelectrode of hematite (α-Fe_2O_3) were deposited onto conducting glass substrates (SnO_2:F; FTO) by using radio frequency (13.56 MHz) plasma CVD and iron pentacarbonyl ($Fe(CO)_5$) as the precursor. The pre-cleaning of substrates prior to the coating involved the following steps: ultrasonic cleaning in de-ionized water; rinsing in iso-propyl alcohol; washing in de-ionized water; drying in air in an oven maintained at 70 °C followed by a final treatment with Ar plasma to remove any persisting adsorbate film.

Deposition of the $Nd_2Sn_2O_7$ layer. After setting the substrate on the disk of the spin-coater, the coating solution (approx. 0.2 ml) was dropped and spin-coated with 600 rev. min^{-1} for 20 s in air. The precursor film specimen was then dried in air at 80 °C for 10 min and the process was repeated 5 times in order to reach the desired thickness and homogeneity.

Electrospinning of $Nd_2Sn_2O_7$ nanofibers. The nanofibers were produced via electrospinning of NdSn-sols. Typically, a solution of 0.353 g of $NdSn(O^tBu)_5Py$ in 15 mL of 2-propanol was mixed under vigorous stirring, followed by the addition of 0.032 mg acetic acid and 600 mg of

polyvinylpyrrolidone (PVP, 1300000 g/mol) as the spinning-aid. As-obtained electrospun nanofibers were subjected to ex-situ annealing at 800 °C for 3 h to obtain a crystalline phase.

Photoelectrochemical Measurement of photoanodes. The photoelectrochemical response of layers was investigated in a quartz PEC cell having our samples as the working photoelectrode, saturated calomel as the reference electrode and Pt as a counter electrode coupled to a potentiostat (PAR, Model: Versa state IV, USA) and an 150 W xenon arc lamp (Oriel). 1 M NaOH was used as the electrolyte throughout the study. The PEC measurements were firstly conducted in the dark. Once the dark measurements were obtained, the photoanodes were measured under light illumination.

Materials Characterization. Room-temperature powder X-ray diffraction (XRD) was obtained on a STOE-STADI MP diffractometer operating in the reflection mode using Cu Kα (λ = 1.5406 Å) radiation. The microstructures of the samples were examined using field-emission scanning electron microscopy (FE-SEM, FEI Nova NanoSEM 430).

AUTHOR INFORMATION

Corresponding Author

*E-mail: sanjay.mathur@uni-koeln.de.

ACKNOWLEDGMENT

The authors gratefully acknowledge the financial support provided by the University of Cologne and the European Commission for partial funding under the contract WIROX n° PIRSE-GA-2011-295216 (Marie Curie Action). We thank David Graf and Markus Schütz for the reproduction of some compounds and for the analytical data.

REFERENCES

(1) Carp, O., *Progress in Solid State Chemistry* **2004,** 32, 33-177.
(2) Mettenbörger, A.; Singh, T.; Singh, A. P.; Järvi, T. T.; Moseler, M.; Valldor, M.; Mathur, S., *International Journal of Hydrogen Energy* **2014,** 39, 4828-4835.
(3) Barreca, D.; Carraro, G.; Gasparotto, A.; Maccato, C.; Sada, C.; Singh, A. P.; Mathur, S.; Mettenbörger, A.; Bontempi, E.; Depero, L. E., *International Journal of Hydrogen Energy* **2013,** 38, 14189-14199.
(4) Singh, A. P.; Mettenbörger, A.; Golus, P.; Mathur, S., *International Journal of Hydrogen Energy* **2012,** 37, 13983-13988.
(5) Warren, S. C.; Voitchovsky, K.; Dotan, H.; Leroy, C. M.; Cornuz, M.; Stellacci, F.; Hebert, C.; Rothschild, A.; Gratzel, M., *Nat Mater* **2013,** 12, 842-849.
(6) Singh, T.; Müller, R.; Singh, J.; Mathur, S., *Applied Surface Science* **2015,** 347, 448-453.
(7) Song, Y.-M.; Dai, J.-Q.; Zhang, H., *Ferroelectrics* **2015,** 478, 106-117.
(8) Wang, S. M.; Lu, M. K.; Zhou, G. J.; Zhou, Y. Y.; Zhang, H. P.; Wang, S. F.; Yang, Z. S., *Materials Science and Engineering: B* **2006,** 133, 231-234.
(9) Xu, Z.-C.; Liu, M.-F.; Lin, L.; Liu, H.; Yan, Z.-B.; Liu, J.-M., *Frontiers of Physics* **2014,** 9, 82-89.
(10) Teraoka, Y.; Torigoshi, K.-i.; Yamaguchi, H.; Ikeda, T.; Kagawa, S., *Journal of Molecular Catalysis A: Chemical* **2000,** 155, 73-80.
(11) Kennedy, B. J.; Hunter, B. A.; Howard, C. J., *Journal of Solid State Chemistry* **1997,** 130, 58-65.
(12) Whinfrey, C. G.; Eckart, D. W.; Tauber, A., *Journal of the American Chemical Society* **1960,** 82, 2695-2697.
(13) Cheng, H.; Wang, L. P.; Lu, Z. G., *Nanotechnology* **2008,** 19, 025706.
(14) Wang, W.; Ning, P. F.; Fang, J. L.; Wang, W. X., *Ceramics International* **2014,** 40, 13841-13845.
(15) Wang, Z. J.; Zhou, G. H.; Zhang, F.; Qin, X. P.; Ai, J. P.; Wang, S. W., *Journal of Luminescence* **2016,** 169, 612-615.
(16) Mao, Y.; Li, G.; Xu, W.; Feng, S., *Journal of Materials Chemistry* **2000,** 10, 479-482.
(17) Zeng, J.; Wang, H.; Zhang, Y.; Zhu, M. K.; Yan, H., *The Journal of Physical Chemistry C* **2007,** 111, 11879-11887.
(18) Zhang, T. T.; Li, K. W.; Zeng, J.; Wang, Y. L.; Song, X. M.; Wang, H., *Journal of Physics and Chemistry of Solids* **2008,** 69, 2845-2851.
(19) Moon, J.; Awano, M.; Maeda, K., *Journal of the American Ceramic Society* **2001,** 84, 2531-2536.
(20) Veith, M.; Mathur, S.; Mathur, C., *Polyhedron* **1998,** 17, 1005-1034.
(21) Meerwein, H.; Bersin, T., *Justus Liebigs Annalen der Chemie* **1929,** 476, 113-150.
(22) Veith, M.; Kunze, K., *Angewandte Chemie International Edition in English* **1991,** 30, 95-97.
(23) Samedov, K.; Aksu, Y.; Driess, M., *Chemistry of Materials* **2012,** 24, 2078-2090.
(24) Veith, M.; Käfer, D.; Koch, J.; May, P.; Stahl, L.; Huch, V., *Chemische Berichte* **1992,** 125, 1033-1042.
(25) Njua, E. Y.; Steiner, A.; Stahl, L., *Inorg Chem* **2010,** 49, 2163-2172.
(26) Veith, M.; Käfer, D.; Huch, V., *Angewandte Chemie International Edition in English* **1986,** 25, 375-377.

(27) Veith, M.; Rosier, R., *Zeitschrift für Naturforschung B* **1986**; 41, 1071-1080.
(28) Veith, M.; Hans, J.; Stahl, L.; May, P.; Huch, V.; Sebald, A., *Zeitschrift für Naturforschung B* **1991,** 46, 403-424.
(29) Shannon, R. t., *Acta Crystallographica Section A: Crystal Physics, Diffraction, Theoretical and General Crystallography* **1976,** 32, 751-767.
(30) Schlafer, J.; Stucky, S.; Tyrra, W.; Mathur, S., *Inorg Chem* **2013,** 52, 4002-4010.
(31) Manning, T. D.; Loo, Y. F.; Jones, A. C.; Aspinall, H. C.; Chalker, P. R.; Bickley, J. F.; Smith, L. M.; Critchlow, G. W., *Journal of Materials Chemistry* **2005,** 15, 3384-3387.
(32) Cleave, A. R., *Atomic scale simulations for waste form applications*. ed.; University of London, London (UK), **2006**.
(33) Subramanian, M.; Aravamudan, G.; Rao, G. S., *Progress in Solid State Chemistry* **1983,** 15, 55-143.
(34) Alemi, A.; Ebrahimi Kalan, R., *Radiation Effects & Defects in Solids* **2008,** 163, 229-236.
(35) Mettenbörger, A.; Gönüllü, Y.; Fischer, T.; Heisig, T.; Sasinska, A.; Maccato, C.; Carraro, G.; Sada, C.; Barreca, D.; Mayrhofer, L., *Nano Energy* **2016,** 19, 415-427.
(36) Bradley, D. C.; Ghotra, J. S.; Hart, F. A., *Journal of the Chemical Society, Dalton Transactions* **1973**, 1021-1023.
(37) Fjeldberg, T.; Hitchcock, P. B.; Lappert, M. F.; Smith, S. J.; Thorne, A. J., *Journal of the Chemical Society, Chemical Communications* **1985**, 939-941.
(38) GmbH, S. C., *Darmstadt, Deutschland* **2005,** X-RED32 1.31.
(39) Farrugia, L. J., *Journal of Applied Crystallography* **1999,** 32, 837-838.
(40) Altomare, A.; Cascarano, G.; Giacovazzo, C.; Guagliardi, A.; Burla, M.; Polidori, G. t.; Camalli, M., *Journal of Applied Crystallography* **1994,** 27, 435-436.
(41) Sheldrick, G. M., *Acta Crystallogr A* **2008,** 64, 112-22.
(42) Spek, A., *Journal of Applied Crystallography* **2003,** 36, 7-13.

For Table of Contents Use Only

Precursor-derived rare earth metal pyrochlores: $Nd_2Sn_2O_7$ nanofibers and thin films as efficient photoabsorbers

Aida Jamil, Johannes Schläfer, Yakup Gönüllü, Ashish Lepcha and Sanjay Mathur*

Synopsis

Nanofibers and thin films of rare earth pyrochlores were produced by electrospinning and spin-coating of chemical sols obtained from mixed-metal single-source precursors that effectively suppress possible phase separation scenarios to deliver single-phase $Ln_2M_2O_7$. Photocatalytic studies demonstrated high activity for $Nd_2Sn_2O_7$ nanofibers when compared to commonly applied TiO_2 nanostructures used as the reference. Moreover $Nd_2Sn_2O_7$ films grown over Fe_2O_3 photoanodes yielded superior efficiency for photoelectrochemical splitting of water in comparison to bare Fe_2O_3 layers, possibly due to higher absorption cross-section and enhanced charge carrier mobilities in $Nd_2Sn_2O_7$//Fe_2O_3 heterojunctions.